

Ultrathin Silicon Nanomembrane in a Tubular Geometry for Enhanced Photodetection

Changhao Xu, Ruobing Pan, Qinglei Guo, Xiang Wu, Gongjin Li, Gaoshan Huang, Zhenghua An, Xiuling Li, and Yongfeng Mei*

Advanced 3D mesostructures have prominent applications in flexible electronics, photonics, mechanics, and biomedicine. Here, 3D tubular silicon photodetectors are demonstrated by self-rolling ultrathin silicon nanomembranes with enhanced broadband photodetection and responsivity. Strain distributions within the unique circular structures are investigated with micro-Raman spectroscopy, while the tensile strain of the rolled-up microtubes can be controlled with the tube diameter by modifying the membrane thickness and etching parameters during the rolled-up process. The tubular photodetector exhibits increased photocurrent and suppressed dark current compared with planar devices over a wide incident angle. This study provides a novel approach to construct high-performance omnidirectional Si-based photodetectors and offers promising prospects for design and manufacture of complex 3D optoelectronic devices.

The recent advances in 3D mesostructures have given rise to a number of intriguing devices that exhibit unique features, which have broad applications in flexible electronics,^[1] photonics,^[2,3] mechanics,^[4] and biomedicine.^[5] Among various fabrication techniques, rolled-up nanotechnology is an innovative method that constructs 3D tubular micro/nanostructures out of planar nanomembranes from the top-down perspective. The geometries and properties of these rolled-up structures could be precisely controlled through strain engineering, which further

inspired applications such as optical resonators,^[6] passive electronic components^[7] microrobotics,^[8] gas detection,^[9] energy storage,^[10] and bioplatfoms.^[11]

Silicon photodetectors have been intensively studied due to its mass production and low cost with standard complementary metal–oxide–semiconductor (CMOS) manufacturing processes.^[12] Traditional silicon nanomembrane (SiNM) detectors face the challenge of low light absorption coefficient, nonperfect response properties and angle-dependent light detection. To overcome these limitations and further promote photodetection performance, alternative materials and methodologies including graphene,^[13] transitional metal dichalcogenides,^[14] surface plasmon polar-

iton^[15] and quantum dot^[16] have been explored as potential candidates. However, these photodetectors are often hindered by instability or high-cost and therefore unfavorable along the path to their commercialization. It is still challenging to fabricate omnidirectional all-Si photodetectors and improve its sensitivity.

In this work we demonstrate that 3D silicon-based photodetectors could be fabricated by rolling up ultrathin silicon nanomembranes (SiNMs). Strain distributions within the circular structure were characterized with micro-Raman spectroscopy of different excitation lasers. The tensile strain in the functional SiNMs could be well manipulated by tuning the strain layer thickness and etching parameters during the rolled-up fabrication process. The optoelectronic performance of 3D tubular Si photodetector was also investigated, exhibiting enhanced broadband photodetection and responsivity, which resulted from increased photocurrent and suppressed dark current. Furthermore, the unique tubular structure enables omnidirectional enhanced sensitivity over a wide incident angle, even without extra light-coupling plasmonics designs or optimized doping patterns.^[17] Our work paves the way for integrating 3D photodetectors with on-chip silicon circuits and opens up possibilities for design and construction of future generations of sophisticated 3D optoelectronic devices.


The schematic illustration of the rolled-up Si photodetector is presented in **Figure 1a**. The device consists of two chromium electrodes on the 20 nm thick SiNM and a 20 μm wide Si channel. We use chromium because Cr could not only serve as the strain layer but also was found to form a perfect Schottky contact with ultrathin SiNM.^[18] The Cr layer was deposited on precleaned SiNM by e-beam evaporation with

C. H. Xu, R. B. Pan, X. Wu, Dr. G. Li, Prof. G. S. Huang, Prof. Y. F. Mei
Department of Materials Science
State Key Laboratory of ASIC and Systems
Fudan University
Shanghai 200433, P. R. China
E-mail: yfm@fudan.edu.cn

Prof. Q. Guo
Center of Nanoelectronics and School of Microelectronics
Shandong University
Jinan 250100, P. R. China

Prof. Z. An
Department of Physics
Fudan University
Shanghai 200433, P. R. China

Prof. X. Li
Department of Electrical and Computer Engineering
Micro and Nanotechnology Laboratory
University of Illinois Urbana–Champaign
208 N. Wright Street, Urbana, IL 61801, USA

 The ORCID identification number(s) for the author(s) of this article can be found under <https://doi.org/10.1002/adom.201900823>.

DOI: 10.1002/adom.201900823

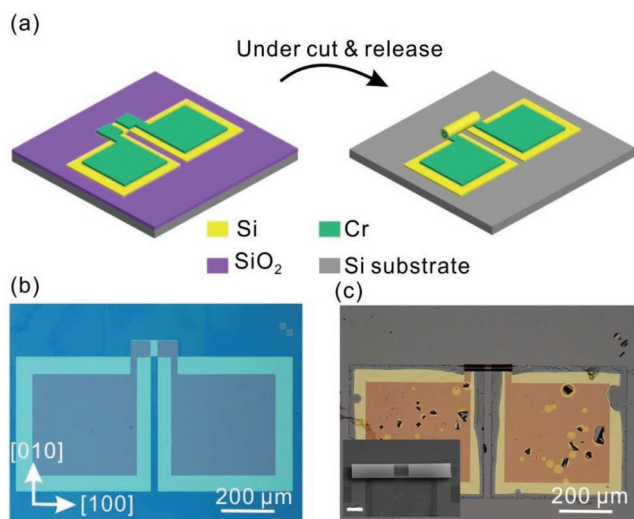


Figure 1. a) Schematic diagram of the fabrication process for a 3D tubular silicon photodetector device. b) Optical image of a planar silicon nanomembrane photodetector. The long side of the planar pattern is defined along $\langle 100 \rangle$ direction. c) Optical image of a 3D tubular silicon photodetector device, inset: SEM of the silicon tube, scale bar: 20 μm .

carefully manipulated growth condition to achieve adequate built-in tensile strain. It is well known that in an anisotropic system the rolling direction is mainly determined by the most compliant direction.^[19] Therefore, the long sides of the patterns were designed to follow the $\langle 100 \rangle$ direction, as demonstrated in Figure 1b. After photolithography and selective wet chemical etching, the buried sacrificial oxide of the planar Si photodetector was selectively etched away to release the Cr/Si nanomembrane from its substrate. Due to the built-in tensile strain in the Cr layer, the bilayer rolls up into a microtube. The optical image and scanning electron microscopy (SEM) image of the rolled-up Si photodetector are shown in Figure 1c.

As reported previously,^[20] basically two parameters control the diameter of the rolled-up tubes: strain gradient and layer thickness. In our experiment, the Si tube diameter can be effectively tuned by modifying the strain layer thickness (i.e., Cr thickness) and underetching time. Typical tube diameters formed out of 25 nm/20 nm Cr/Si bilayer were measured to be $\approx 15 \pm 1 \mu\text{m}$. When increasing the Cr thickness to 40 nm, the tube diameters accordingly increased to $\approx 20 \pm 1 \mu\text{m}$ (see Figure S1, Supporting Information). Increasing the thickness of Cr although contributes to a larger initial strain, it also drastically strengthens the rigidity of the bilayer system, resulting in a larger tube. Meanwhile, tube diameter modulation could also be achieved by underetching time. During this process the tube was released while the edges of the tube was restricted by the fixed electrode pad, so enhancing the etching time could lead to strain relaxation in the tubular structure and thereby result in a larger diameter. SEM images of the corresponding samples with different diameters by extending etching time are shown in Figure S2 in the Supporting Information.

Previous studies have pointed out that uniaxial strain was generated along the rolled-up direction due to the bending effect.^[21] When the Cr/Si bilayer rolls up into a microtube, the internal strain also redistributed along the vertical direction.

To characterize the strain distributions in the curved SiNM, the rolled-up Si tubes were measured with micro-Raman spectroscopy with two excitation lasers. The power of both excitation lasers were turned down to 3 mW in our measurement to minimize the local heating effect.^[22,23] It should be noted that the penetration depth of Raman spectroscopy is determined by the detection wavelength. For the 325 nm laser, the maximum penetration depth in silicon is 8.16 nm, as for the 514 nm laser the penetration depth reaches $\approx 1 \mu\text{m}$, which far exceeds the thickness of SiNMs, as shown in Figure 2a. Therefore, the Raman signal of 325 nm laser reflects the surface strain of the SiNM, while the signal of 514 nm represents an average value of the bulk SiNM.^[24] The corresponding Raman spectrums of planar nanomembranes and rolled-up Si tubes obtained with 325 and 514 nm laser is shown in Figure 2b. The tube diameter is measured to be 15 μm , and the corresponding Raman shift is $\approx 3.8 \text{ cm}^{-1}$.

The uniaxial strain in the SiNM can be calculated from the empirical formula^[25]

$$(\omega_{\text{bulk}} - \omega_{\text{strained}}) = -813\varepsilon \quad (1)$$

where ω (cm^{-1}) represents the peak positions for bulk silicon and strained SiNMs, 813 (cm^{-1}) is the strain-phonon coefficient, and ε (%) is the strain. Consequently, tensile strain in the rolled-up SiNM is confirmed by the downshift of Raman peak to lower frequencies with respect to the planar SiNMs. The strain distribution along the radical direction of a 15 μm silicon tube excited by 325 and 514 nm lasers is thereby calculated and plotted with three data group statistics for each in Figure 2c.

According to the band bending theory,^[26] the inner and outer surface experience compressive and tensile strain, respectively. Thus the uniaxial tensile strain is also analyzed by theoretical calculation from the following equation^[27]

$$R = \frac{(d_{\text{strain}} + d_{\text{relax}})^3}{6\varepsilon(1 + \nu)d_{\text{strain}}d_{\text{relax}}} \quad (2)$$

where d is the layer thickness, R is the radius of the released Si tubes, ν is the Poisson ratio of the bilayer materials. The theoretical strain distribution can therefore be approximated as linear dependence along the radial direction of the tube, as shown in Figure 2c. The calculated theoretical strain agrees well with the experimental observations, where minor discrepancy could result from two possible reasons: i) strain variation along the vertical direction of the bilayer and ii) local heating effect owing to the irradiation of laser power. Figure 2d summarizes the statistics of Raman shift due to Si-Si vibration mode from unreleased SiNM and released Si tubes of different diameters, in which we applied a numerical fitting and the result is plotted as red curve in order to approach the ideal Raman shift, reducing fluctuations of local heating effect.^[28] As the diameter of the Si tubes decreases from 20 to 14 μm , the strained Cr layer is capable of stretching more intensively, leading to a higher tensile strain state.

To investigate the photoresponse of the fabricated 3D tubular Si photodetectors, the current-voltage characteristics were measured. The incident light source was radiated by the white light and 980 nm laser successively. The I - V curves under white light of both the rolled-up silicon tubes and referential planar nanomembranes are clearly illustrated in Figure 3a,

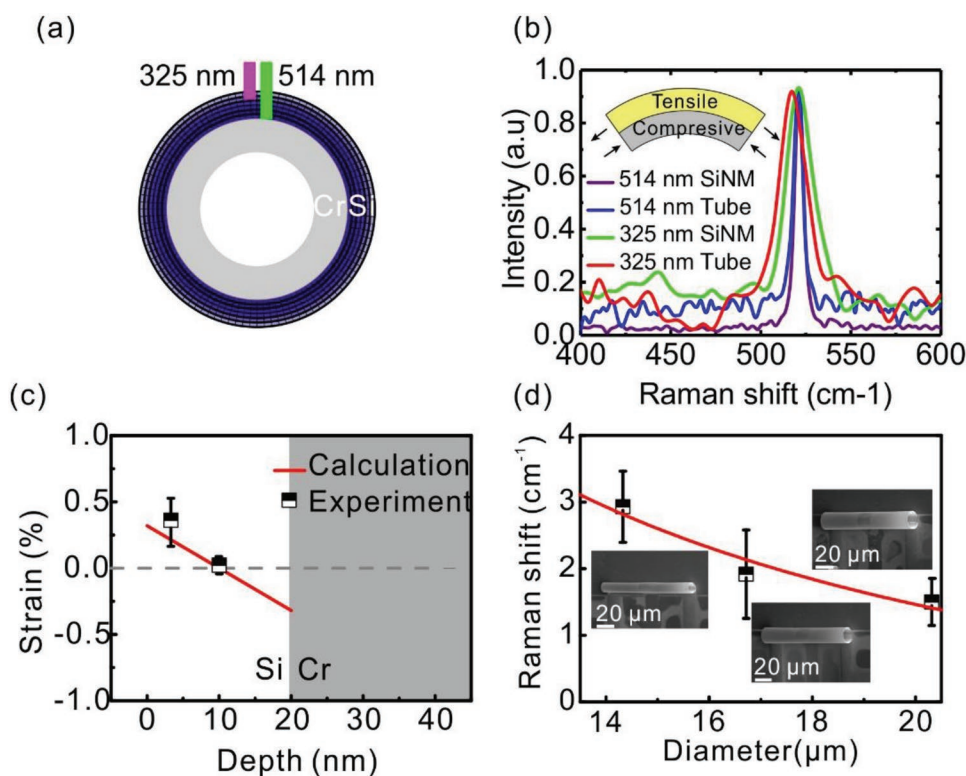


Figure 2. a) Schematic of the penetration depth of the lasers with wavelength 325 and 514 nm on rolled-up silicon tubes. b) Raman spectroscopy of tubes and planar SiNMs under the two excitation wavelengths. c) Experimental and calculated strain analysis in the silicon tube. d) Raman shift statistics of silicon tubes with different diameters, inset: SEM image of Si microtubes with different tube diameters.

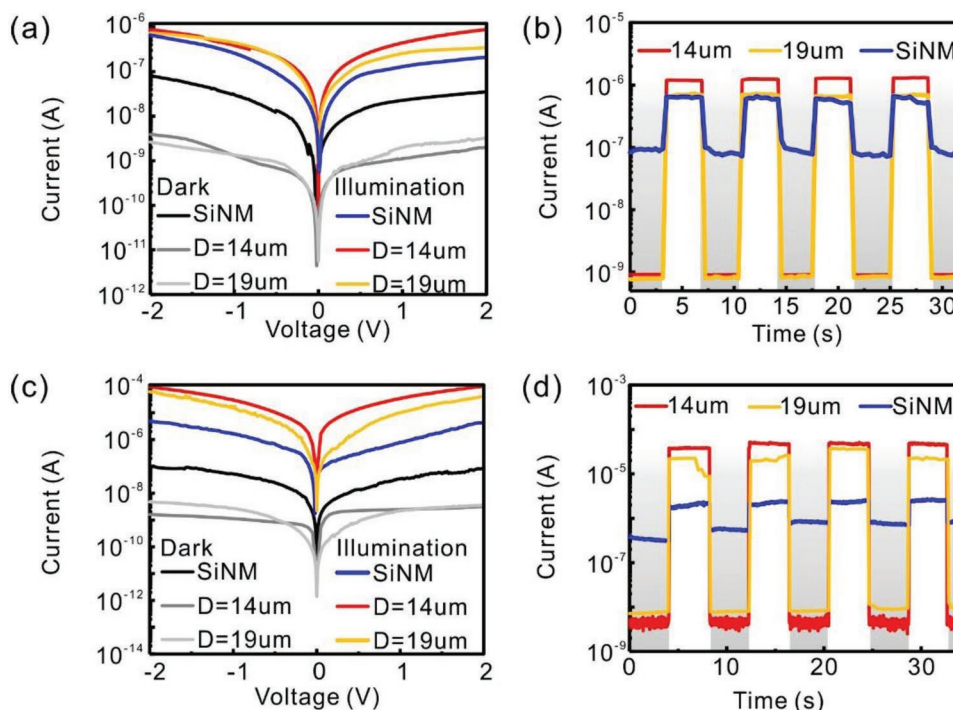


Figure 3. a) Current–voltage characteristics of unreleased SiNMs and released Si tubular photodetectors with different tube diameters illuminated by white light. b) On–off ratio of Si tubular photodetectors with different tube diameters illuminated with white light. c) Current–voltage characteristics of unreleased SiNMs and released Si tubular photodetectors illuminated by 980 nm laser. d) On–off ratio of Si tubular photodetectors with different tube diameters illuminated by 980 nm laser.

showing that enhanced I_{on}/I_{off} ratio reaches $\approx 10^3$ times larger than unreleased SiNMs, which results from increased light-coupling capability of the tubular structure and suppressed dark current. Additionally, the photocurrent further increases with reduced tube diameter. Figure 3b gives the detailed I_{on}/I_{off} ratio of both the tubular (14 and 19 μm diameter, respectively) and planar photodetector under a fixed positive working voltage of 2 V. Similarly, Figure 3c,d gives the photoresponse of tubular Si photodetectors and planar SiNMs under a 980 nm laser. As the laser power is much higher than the white light one's, both tubular and planar SiNMs sensors display higher I_{on}/I_{off} ratio, the maximum I_{on}/I_{off} ratio of which reach almost 10^5 and 10^2 , respectively, as shown in Figure 3c. Under both white light and 980 nm illumination, the enhanced photodetection properties of tubular SiNM devices originates from suppressed dark current and increased photocurrent compared with that of planar SiNM devices, whose detailed mechanism is proposed in Figure 5.

Traditional planar photodetectors face the challenge that the detection sensitivity is strongly affected by the incident light direction, which is unfavorable for omnidirectional detection applications. To investigate the directional detection, a 980 nm laser was used as the illumination source, which rotated around the 3D tubular photodetectors and the planar ones, as demonstrated in Figure 4a. The rolled-up tubular photodetector exhibits a stable photocurrent and remained a high enhancement over a wide incident angle from 20° to 160° , as shown in Figure 4b. The I_{on}/I_{off} ratio of tubular and planar SiNM devices at corresponding incident angle is shown in Figure 4b. Compared with planar geometries (black curves in Figure 4b), our 3D tubular photodetector presents an omnidirectional feature due to the unique symmetric circular light-coupling geometry. Considerably larger enhancement was observed especially for small angle detection, as shown in $<60^\circ$ and $>120^\circ$ regions in Figure 4c.

As described above, a dramatic increase of photocurrent and decrease of dark current is observed in the 3D tubular Si photodetectors with regard to planar Si photodetectors. The mechanism of suppressed dark current in the rolled-up structure may be attributed to two possible factors: increased surface charge-trapping states and piezoresistance effect, as shown in Figure 5a. High density surface states could be generated on both the inner and outer surface of the tube wall and act as charge traps.^[29,30] The increment of charged surface states could trap and deplete mobile charge carriers of Si and strongly influence the carrier density,^[31] and as a result the surface of the tube becomes depletion layer, which decreases the conductivity of rolled-up tubes.^[32] In addition, the increased surface states at the interface between Si and Cr enlarged the Schottky barrier height of the contact,^[33,34] which further decreased the carrier density in rolled-up structure. As discussed above, uniaxial strain in the SiNM tunes its electronic structure. The uniaxial stress also affects the resistivity of semiconductors by piezoresistance effect.^[35] Internal tension induces upward band bending, which results in the change of number as well as the mobility of charge carriers. When the carrier transport direction is perpendicular to the strain direction, the resistivity was reported to be enhanced by the compressive strain in the inner surface of tubular structure.^[24,31] Consequently, the effective conducting layer will be shrunken and sandwiched by two

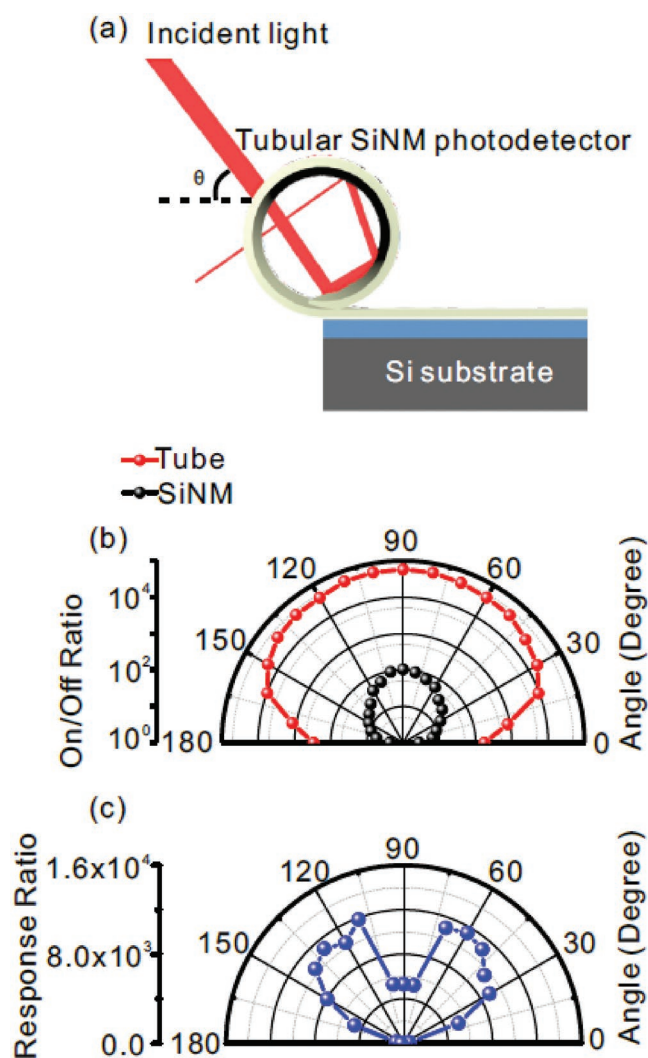


Figure 4. a) Schematic diagram of Si tubular photodetectors illuminated with infrared laser. b) On/off ratio of Si tubular photodetectors and planar SiNMs. c) Comparative response ratio between tubular and planar SiNMs photodetector.

depletion layers as schematically illustrated in the top panel of Figure 5a, thus leading to decreased conductivity in rolled-up Si tubes, of which the statistic dark current of different tube diameter and planar SiNM was shown in Figure 5b. Under rolled-up condition, dark current decreased over one order magnitude compared with that of planar SiNM. And with the tube diameter decreasing, the corresponding dark current was further suppressed. As Figure 3 depicted, 3D tubular structure not only suppressed dark current but also implemented higher photoresponse. To elucidate the photocurrent enhancement mechanism, a simulational electrical field of the light-coupling distribution at the 980 nm wavelength was carried out, as shown in Figure 5c. When the incident light transmits through the hollow tube, part of the light is trapped and bounced repeatedly within the inner walls of the tubular structure (see Figure 4a), a portion of which will be absorbed and induces photogenerated current, while planar designs lack such trapping properties.^[36] Therefore, the 3D tubular structure significantly confined

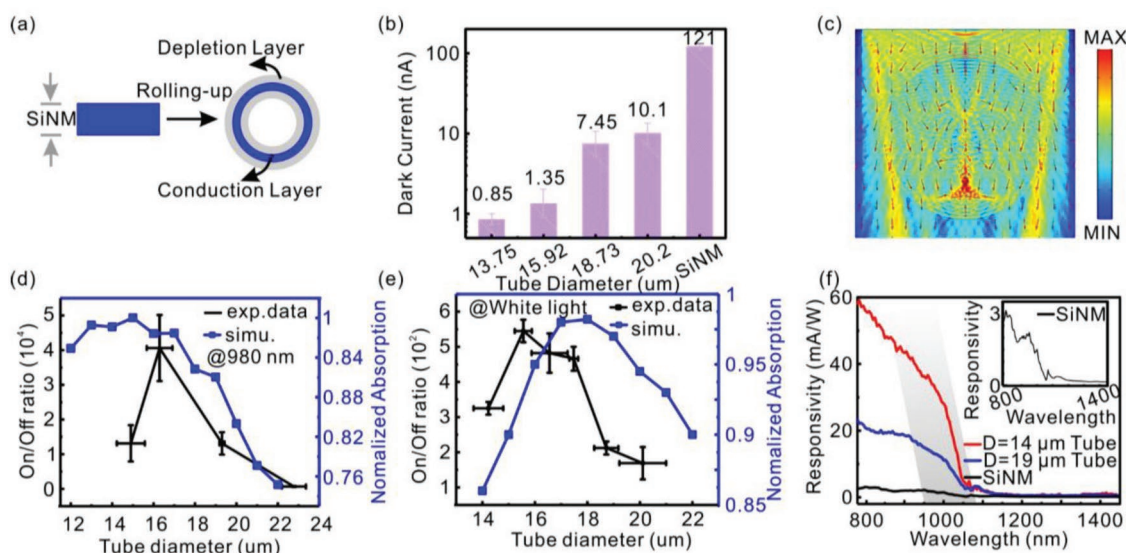


Figure 5. a) Schematic of depletion layer generated through rolled-up process. b) Statistic dark current versus different average tube diameter with regarding to the initial SiNM. c) Numerical simulation of the light-coupling distribution in a rolled-up silicon tube. d,e) On/off ratio of Si tubular photodetectors and planar SiNMs at 980 nm laser and white light, respectively. f) Responsivity spectrum from 780 to 1450 nm of tubular photodetectors with 14/19 μm and planar SiNM photodetector.

electro-magnetic field compared with conventional planar designs. The compared simulational electrical field of SiNM was shown in figure S5 in the Supporting Information. To elucidate the relationship between photoresponse of different tube dimensions, the statistics of $I_{\text{on}}/I_{\text{off}}$ ratio versus tube diameter at 980 nm and white light with corresponding absorption was shown in Figure 5d,e. The $I_{\text{on}}/I_{\text{off}}$ ratio and corresponding absorption go up nonmonotonically under certain illumination with the tube diameter monotonically increasing, which means reflecting times within the unique symmetric tubular geometry is strongly affected by tube diameter. In addition, there exists some mismatch between experiment data and absorption simulation because $I_{\text{on}}/I_{\text{off}}$ ratio is the coupled result of both absorption and dark current suppression. Nevertheless, similar tendency between $I_{\text{on}}/I_{\text{off}}$ ratio and simulation absorption was observed. The maximum $I_{\text{on}}/I_{\text{off}}$ ratio of Si tube reached 4×10^4 at 980 nm in our experiment.

To explore photodetection performance of different wavelengths, the 3D tubular Si photodetectors of different diameters were tested under a supercontinuum laser with a variable wavelength from 780 to 1450 nm. The results are identified by red and blue curves in Figure 5f, with respect to the black curve of planar SiNM, in which the chosen tube devices coincided with those in Figure 3. It is clearly shown that the responsivity of our silicon tubes is about an order of magnitude higher than that of unreleased SiNM, with a nearly wavelength independent enhancement. The photocurrent response of both the rolled-up silicon tube and the reference SiNM decreases after reaching the value of Si energy bandgap (≈ 1100 nm). Nevertheless, an enhancement at the sub-bandgap region (>1100 nm) is observed in the spectra. One possible explanation is related to surface states. As is described above, the increased surface states and roughness induced by rolled-up process in SiNM tube may act as

an efficient absorption source for infrared light, without the assistance of extra light-couplers.^[37]

In summary, rolled-up 3D tubular Si photodetectors have been successfully fabricated out of ultrathin SiNM via the self-rolled-up membrane nanotechnology. Uniaxial tensile strain is well controlled by tuning the tube diameter during the rolled-up process, which is experimentally verified by micro-Raman spectroscopy. The strain distribution based on the Raman shift agrees well with the bending theory. The strain-engineered tubular SiNM photodetector exhibited $\approx 10^3$ times enhanced photoresponsivity than the planar counterpart. The increased photocurrent and suppressed dark current can be attributed to surface charge-trapping states and piezoresistance effect. The 3D tubular structures demonstrated an omnidirectional intensified detection over a wide incident angle. A numerical model was built to explain the enhancement mechanism by multiple reflections within the tubular structure. Photocurrent spectroscopy measurement revealed a broad-spectrum enhancement and an infrared absorption in our tubular photodetectors. Our work provides a convenient route to design and fabricate CMOS-compatible 3D photodetectors and other complex on-chip optoelectronic devices.

Experimental Section

Fabrication of Rolled-Up Si Tubes: The silicon on insulator (SOI) wafer with Si/SiO₂ thicknesses of 20/150 nm was purchased from SOITEC Inc. The SOI was initially cleaned using 10% dilute hydrofluoric acid (HF) acid to remove the native oxide on the surface. Chromium layers of different thicknesses were deposited by e-beam evaporation at a constant rate 2 \AA s^{-1} . Photoresist (AZ 5214) was spin coated at a speed of 3500 r min^{-1} , after which long side of the patterns were aligned to be parallel with $\langle 100 \rangle$ direction of the Si substrate. After standard photolithography (Heidelberg, uPG501) to isolate devices on the chip, wet chemical

etching was used to remove the excess Cr layer in a standard chromium etchant, after which reactive ion etching was performed to expose the buried oxide under the following conditions: 18 sccm CHF₃ flow rate, 35 sccm SF₆ flow rate, 30 mT chamber pressure, and 50 W power for 60 s. A second photolithography was subsequently performed to pattern the source, drain, and channel of the device. Then, the standard chromium etchant was used again to form a 20 μm wide silicon channel of the device. The planar photodetector was subsequently immersed in a 49% HF to remove the buried oxide, and the strained silicon nanomembrane was released and rolled up to form a microtube. Finally, critical point drying was applied to clean the residues and preserve the tubular microstructure.

Raman Characterization: The strain analysis of Si tubes was carried out by micro-Raman spectrometer (HORIBA JY HR800) with two light sources of wavelength 514 nm argon laser and 325 nm He–Cd laser, respectively. The power of the excitation laser was set to be 3 mW with a spot size of 1 μm.

SEM Characterization: The morphology of the tubes was characterized by SEM (Zeiss Sigma 300), with operating voltage of 5 kV.

Photoelectric Measurement: Electrical measurements of the photodetectors were carried out in a probe station with source measurement units (Keithley 4200) at room temperature. The photodetectors were illuminated with a 980 nm irradiation laser and super-continuum source ranging from 400 to 1450 nm (YSL Photonics SC-PRO).

Supporting Information

Supporting Information is available from the Wiley Online Library or from the author.

Acknowledgements

C.H.X. and R.B.P. contributed equally to this work. This work was supported by the Natural Science Foundation of China (Grant Nos. 51711540298, 61628401, U1632115, and 51475093), Science and Technology Commission of Shanghai Municipality (Grant No. 17JC1401700), the National Key Technologies R&D Program of China (Grant No. 2015ZX02102-003), the Program of Shanghai Academic Research Leader (19XD1400600) and the Changjiang Young Scholars Program of China. Part of the experimental work was conducted in Fudan Nanofabrication Laboratory.

Conflict of Interest

The authors declare no conflict of interest.

Keywords

photodetector, rolled-up nanotechnology, silicon nanomembrane

Received: May 15, 2019

Revised: July 15, 2019

Published online: August 12, 2019

- [1] Y. Zhang, F. Zhang, Z. Yan, Q. Ma, X. Li, Y. Huang, J. A. Rogers, *Nat. Rev. Mater.* **2017**, *2*, 17019.
 [2] C. M. Soukoulis, M. Wegener, *Nat. Photonics* **2011**, *5*, 523.
 [3] E. Song, Q. Guo, G. Huang, B. Jia, Y. Mei, *ACS Appl. Mater. Interfaces* **2017**, *9*, 12171.
 [4] B. Xu, B. Zhang, L. Wang, G. Huang, Y. Mei, *Adv. Funct. Mater.* **2018**, *28*, 1705872.

- [5] S. M. Won, E. Song, J. Zhao, J. Li, J. Rivnay, J. A. Rogers, *Adv. Mater.* **2018**, *30*, 1800534.
 [6] Z. Tian, L. Zhang, Y. Fang, B. Xu, S. Tang, N. Hu, Z. An, Z. Chen, Y. Mei, *Adv. Mater.* **2017**, *29*, 1604572.
 [7] W. Huang, J. Zhou, P. J. Froeter, K. Walsh, S. Liu, M. D. Kraman, M. Li, J. A. Michaels, D. J. Sievers, S. Gong, X. Li, *Nat. Electron.* **2018**, *1*, 305.
 [8] Y. Mei, A. A. Solovev, S. Sanchez, O. G. Schmidt, *Chem. Soc. Rev.* **2011**, *40*, 2109.
 [9] B. Xu, Z. Tian, J. Wang, H. Han, T. Lee, Y. Mei, *Sci. Adv.* **2018**, *4*, p8203.
 [10] H. Ji, X. Wu, L. Fan, C. Krien, I. Fiering, Y. Guo, Y. Mei, O. G. Schmidt, *Adv. Mater.* **2010**, *22*, 4591.
 [11] G. Huang, Y. Mei, D. J. Thurmer, E. Coric, O. G. Schmidt, *Lab Chip* **2009**, *9*, 263.
 [12] K. J. Yu, L. Gao, J. S. Park, Y. R. Lee, C. J. Corcoran, R. G. Nuzzo, D. Chanda, J. A. Rogers, *Adv. Energy Mater.* **2013**, *3*, 1401.
 [13] Z. Chen, X. Li, J. Wang, L. Tao, M. Long, S. Liang, L. K. Ang, C. Shu, H. K. Tsang, J. Xu, *ACS Nano* **2017**, *11*, 430.
 [14] J. Deng, Z. Guo, Y. Zhang, X. Cao, S. Zhang, Y. Sheng, H. Xu, W. Bao, J. Wan, *IEEE Electron Device Lett.* **2019**, *40*, 423.
 [15] T. Matsui, Y. Li, M. M. Hsu, C. Merckling, R. F. Oulton, L. F. Cohen, S. A. Maier, *Adv. Funct. Mater.* **2018**, *28*, 1705829.
 [16] M. Zhang, L. Wang, L. Meng, X. Wu, Q. Tan, Y. Chen, W. Liang, F. Jiang, Y. Cai, H. Zhong, *Adv. Opt. Mater.* **2018**, *6*, 1800077.
 [17] M. D. Kelzenberg, S. W. Boettcher, J. A. Petykiewicz, D. B. Turner-Evans, M. C. Putnam, E. L. Warren, J. M. Spurgeon, R. M. Briggs, N. S. Lewis, H. A. Atwater, *Nat. Mater.* **2010**, *9*, 239.
 [18] E. Song, W. Si, R. Cao, P. Feng, I. Mönch, G. Huang, Z. Di, O. G. Schmidt, Y. Mei, *Nanotechnology* **2014**, *25*, 485201.
 [19] F. Cavallo, M. G. Lagally, *Soft Matter* **2010**, *6*, 439.
 [20] Y. Mei, G. Huang, A. A. Solovev, E. B. Ureña, I. Mönch, F. Ding, T. Reindl, R. K. Y. Fu, P. K. Chu, O. G. Schmidt, *Adv. Mater.* **2008**, *20*, 4085.
 [21] Q. Guo, M. Zhang, Z. Xue, J. Zhang, G. Wang, D. Chen, Z. Mu, G. Huang, Y. Mei, Z. Di, X. Wang, *AIP Adv.* **2015**, *5*, 37115.
 [22] S. Piskanec, M. Cantoro, A. C. Ferrari, J. A. Zapien, Y. Lifshitz, S. T. Lee, S. Hofmann, J. Robertson, *Phys. Rev. B* **2003**, *68*, 241612R.
 [23] M. J. Süess, R. A. Minamisawa, R. Geiger, K. K. Bourdelle, H. Sigg, R. Spolenak, *Nano Lett.* **2014**, *14*, 1249.
 [24] Q. Guo, G. Wang, D. Chen, G. Li, G. Huang, M. Zhang, X. Wang, Y. Mei, Z. Di, *Appl. Phys. Lett.* **2017**, *110*, 112104.
 [25] G. Sun, M. Zhang, Z. Xue, Q. Guo, D. Chen, Z. Mu, L. Dong, X. Wang, Z. Di, *Appl. Phys. Lett.* **2014**, *105*, 193505.
 [26] Z. Suo, E. Y. Ma, H. Gleskova, S. Wagner, *Appl. Phys. Lett.* **1999**, *74*, 1177.
 [27] R. Songmuang, C. Deneke, O. G. Schmidt, *Appl. Phys. Lett.* **2006**, *89*, 223109.
 [28] X. Wu, Z. Tian, H. Cong, Y. Wang, R. Edy, G. Huang, Z. Di, C. Xue, Y. Mei, *Nanotechnology* **2018**, *29*, 42.
 [29] P. P. Zhang, E. P. Nordberg, B. Park, G. K. Celler, I. Knezevic, P. G. Evans, M. A. Eriksson, M. G. Lagally, *New J. Phys.* **2006**, *8*, 200.
 [30] F. Cavallo, R. Songmuang, O. G. Schmidt, *Appl. Phys. Lett.* **2008**, *93*, 143113.
 [31] N. V. Demarina, D. A. Grützmacher, *Appl. Phys. Lett.* **2011**, *98*, 192109.
 [32] M. G. Lagally, *MRS Bull.* **2007**, *32*, 57.
 [33] W. Monch, *Rep. Prog. Phys.* **1990**, *53*, 221.
 [34] D. Connelly, P. Clifton, *J. Appl. Phys.* **2008**, *103*, 74506.
 [35] C. S. Smith, *Phys. Rev.* **1954**, *94*, 42.
 [36] J. B. Kim, P. Kim, N. C. Pégard, S. J. Oh, C. R. Kagan, J. W. Fleischer, H. A. Stone, Y. Loo, *Nat. Photonics* **2012**, *6*, 327.
 [37] I. Goykhman, B. Desiatov, J. Khurgin, J. Shappir, U. Levy, *Opt. Express* **2012**, *20*, 28594.